Computing Pressure Fields over Laboratory Water Waves Using Particle Image Velocimetry Data

Christoph Sven Funke

Advisor: Mary-Louise Timmermans

Second Reader: Jeff Carpenter

May 1st, 2019

A Senior Thesis presented to the faculty of the Department of Geology and Geophysics, Yale University, in partial fulfillment of the Bachelors Degree.

Computing Pressure Fields Over Laboratory Water Waves Using Particle Image Velocimetry Data

Christoph Sven Funke

Abstract

For over a century, scientists have been studying how wind drives water waves. While multiple wave-growth theories exist, these theories are hard to verify empirically. This is because empirical pressure fields over water are difficult to measure directly. In this paper, I use laboratory particle image velocimetry data to compute the first ever empirically derived pressure fields over water waves. I compute phase average pressure fields for wind-driven waves under four different wind speeds ($U_{10} = 0.86$ m s^{-1}, 2.19 m s^{-1}, 5.00 m s^{-1} and 9.41 m s^{-1}). The pressure fields close the momentum budget to within 10% of total stress. At low wind speeds ($U_{10} = 2.19$ m s^{-1}), the phase average pressure field is roughly 90° out of phase with the water surface. This is optimal for doing work on the water. Wave growth at this wind speed is driven primarily by a high pressure region on the windward side of the wave that is caused by high linear strain and shear strain in the air flow. For the two highest wind speed cases ($U_{10} = 5.00$ m s^{-1} and 9.41 m s^{-1}) , the phase average pressure field is out of phase with the wave. High pressure is found in the wave trough and low is found on the wave crest. The low pressure region on the wave crest is driven by high vorticity in the flow. It is skewed slightly toward the leeward side of the wave, allowing work to be done on the water wave.

Contents

1 Introduction **3**

1.1 Theories of Wave Growth 3

1.2 Computing Pressure from PIV Data 5

1.3 Overview 6

2 Data **7**

3 Methodology **9**

3.1 Poisson Approach 9

3.2 Numerical Procedure 10

3.3 Phase Average 11

3.4 Boundary Conditions 13

3.4.1 Method 1 13

3.4.2 Method 2 14

4 Program Validation: Comparison LES Results **15**

5 Results and Discussion **17**

5.1 Phase Average Pressure Fields 17

5.2 Form Drag and Viscous Stress Profiles 20

5.3 Analysis of Phase Average f 24

6 Conclusion **29**

7 Acknowledgments **31**

Appendices **32**

1 Introduction

The exact mechanism by which water waves grow remains poorly understood and has been subject to research for over 100 years. While several theories of wave growth exist, these theories are hard to verify due to difficulties measuring full spatially-resolved pressure fields over water waves. In this paper, I demonstrate that laboratory particle-image velocimetry data can be used to compute empirical pressure fields over water waves. In the future, such data can be used to verify wave growth theories and investigate in detail atmosphere ocean interactions.

1.1 Theories of Wave Growth

Helmholtz (1868) and Thompson (1871) develop the most basic theory of wave formation by their work on the Kelvin-Helmholtz instability. When two fluids with different densities flow past each other at different speeds, an instability arises at the fluid interface that can lead to wave growth. While setting good foundation for future wave growth theories, the Kevlin-Helmholtz instability inaccurately describes wave growth. According to the theory, a minimum windspeed of 6.6 m s^{-1} is necessary to overcome surface tension and create ripples in a quiescent water surface (Thompson, 1871). In reality however, ripples are observed in wind speeds as low as 1.1 m s^{-1} (Jeffreys, 1925).

To address these shortcomings, Jeffreys (1925) develops a new hypothesis of wave growth. First, Jeffreys shows that any accurate wave growth theory must treat the airflow as rotational and thus take into account turbulence. Next, Jeffreys proposes the sheltering hypothesis of wave growth. According to this theory, airflow separates from the water surface near the wave crest. Impaction on the subsequent wave causes wind to push more strongly against the windward side of the wave than the sheltered leeward side of the wave. This creates a relatively high pressure region on the windward side of the

wave that drives wave growth. While Jeffrey's sheltering hypothesis can be tuned to match observed properties of water waves, it relies heavily on a numerical "sheltering coefficient" which cannot be calculated (Miles, 1957). Attempted measurements of the sheltering coefficient on solid wave models suggest that sheltering is not strong enough to cause wave growth (Phillips, 1957).

Eckart (1953) and Phillips (1957) investigate how random fluctuations in pressure caused by wind blowing over a quiescent surface can cause wave growth. Phillips describes a type of resonance between the random pressure fluctuations and water waves by which waves can grow very quickly. The Phillips mechanism is currently still viewed as one of the leading theories on initial wave growth from a quiescent surface.

Finally, Miles (1957) investigates a mechanism for wave generation by a parallel shear flow $U(y)$. Given a wave speed c, Miles concludes that the rate of wave growth is proportional to the second derivative $U''(y)$ at the height where the wind speed equals c. Miles' theory correctly predicts that the onset of wave formation occurs at wind speeds of around 1 m s^{-1}.

While there has been a lot of work done on developing theories of wave growth, these theories are hard to verify. Several studies have attempted to use direct numerical simulations (DNS) to investigate turbulent airflow over water waves (Sullivan et al., 2018; Yang et al., 2018; Yang and Shen, 2010; Sullivan et al., 2000). True verification of wave growth theories, however, requires detailed measurments of velocity fields and pressure fields over ocean waves. So far, no such measurements exist. Recently, however, Buckley and Veron (2016) uses particle image velocimetrey (PIV) to obtain velocity fields over laboratory water waves with a horizontal and vertical resolution of under 200 μm. PIV is a technique in which tracer particles are injected into an airflow, illuminated using lasers, and repeatedly photographed with high resolution cameras (Buckley and Veron, 2016). The particles can then be correlated between successive pictures to obtain estimates of airflow veloc-

ity. These data provide the first insight into verifying existing wave growth theories. To date, however, no empirically derived pressure fields over water waves have ever been published.

1.2 Computing Pressure from PIV Data

Direct measurement of pressure in airflows is difficult. Traditionally, surface pressure measurements require orifices connected to microphones or transducers (Van Oudheusden, 2013). More recently, pressure-sensitive paint has been developed to assist pressure measurments along a surface (Klein et al., 2005). Neither of these methods, however, can be applied to measure air pressure over water waves since wave surfaces are irregular, moving boundaries. Recent research, predominantly in engineering fields, has investigated ways in which pressure fields can be calculated from high resolution PIV data. PIV has the unique capability of capturing velocity fields in unsteady flows. Van Oudheusden (2013) presents a review paper on the topic. In this section, I briefly summarize developments pertaining to using PIV data in field experiments.

Schwabe (1935) pioneered the use of flow images to compute pressure. He used cinematographic recordings of aqueous flow around a cylinder to deduce the pressure field in the flow. Being in a time before digital image processing or computers, Schwabe's method relied on lengths of streaklines of tracer particles to determine flow directions and speeds. He integrated along streamlines using the Bernoulli equation to obtain the pressure distribution within the fluid. While crude, Schwabe's results were qualitatively reasonable. They mark the beginning of pressure computation for empirical velocity data.

Willert and Gharib (1991) digitalized PIV image processing, which led to a massive expansion of PIV use. One of the first use of digital PIV to compute pressure was by Jakobsen et al. (1997). They used PIV to compute pressure and acceleration within water waves hitting a solid boundary. They

focus entirely on the water itself, however, and not on the air above the water. Since then, many other papers use PIV to compute pressure fields (Baur, 1999; Liu and Katz, 2006; Murai et al., 2007).

In order to calculate pressure fields from PIV data, several approaches are possible. The most basic approach is to use the Bernoulli relationship, as done by Schwabe (1935). Alternate approaches involve solving the pressure Poisson equation (Fujisawa et al., 2005) or spatial integration of the Navier Stokes equations (Baur, 1999; Liu and Katz, 2006). In a comparative study of the three methods, Murai et al. (2007) find the Bernoulli approach is inaccurate and does not give realistic pressure fields. This is because turbulence within the flow violates the steady-state assumption of the Bernoulli equation. The other two approaches give qualitatively similar results. The pressure Poisson method was found to be most robust to noise in the data but is sensitive to the choice of boundary conditions. On the other hand, the spatial integration method is more sensitive to noise in the data but does not require exact boundary conditions. In order to use the spatial integration approach, however, the material derivative $\mathrm{D}\mathbf{v}/\mathrm{D}t$ must be known in the flow. Measuring the material requires a PIV setup that takes enough back-to-back photographs to estimate not only the velocity field, but also how it changes in time ($\partial\mathbf{v}/\partial t$). While possible, this is technologically more difficult. In this paper, I thus use the pressure Poisson method for determining pressure.

1.3 Overview

I begin this paper by summarizing the PIV data I use to compute the pressure fields over water waves. Then, I outline the pressure Poisson approach of computing pressure and describe the numerical methods I use to solve the pressure Poisson equation. I verify my method by running the Poisson solver on large eddy simulation (LES) output data and comparing my computed pressure fields with those from the LES simulation. Next, I investigate the phase average pressure field over wind-driven water waves for three differ-

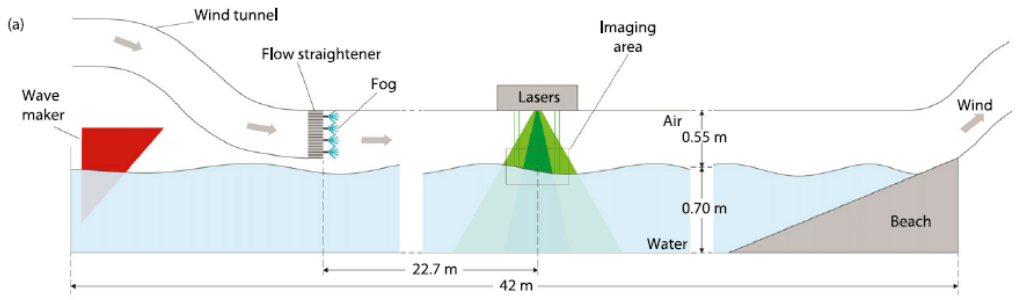

Figure 1: Schematic diagram of the experimental setup. Image modified from Buckley and Veron (2016)

ent wind speeds: $U_{10} = 0.86$ m s^{-1}, 2.19 m s^{-1}, 5.00 m s^{-1}, and 9.41 m s^{-1}. Here, U_{10} refers to the mean horizontal wind speed at an altitude of 10 m above the water surface. I further verify these pressure fields by computing the average form drag over water waves and comparing it with the form drag predicted by law of the wall theory. Finally, in the last section, I describe how interaction between strain and vorticity in different regions of the flow lead to each the observed pressure fields.

2 Data

The data used in this experiment consist of PIV measurements collected by Buckley and Veron (2016) in a large wind-wave current tank at the Air Sea Interaction Laboratory of the University of Delaware. Fig. 1 shows a schematic diagram of the experimental setup. Buckley and Veron (2016) use a combination of PIV and Laser Induced Floresence techniques to measure air particle motions within, on average, 100 µm of the water surface. The final data consist of two-dimensional velocity fields of the airflow over wind-driven water waves. Measured are instantaneous snapshots of horizontal velocity u and vertical velocity w, from which I can compute gradients $\partial u/\partial x$, $\partial u/\partial z$, $\partial w/\partial z$, and $\partial w/\partial x$. The final, processed data are on a square grid

with grid spacing 186 μm. The total length of the grid is 18 cm by 8 cm, corresponding to 981 grid points in the horizontal direction and roughly 350 grid points in vertical direction. The PIV cameras operated at 14.4 frames per second, thus yielding 7.2 velocity estimates per second. The frequency of these velocity estimates is not enough to accurately compute the material acceleration ($\mathrm{D}\mathbf{v}/\mathrm{D}t$). Figure 2 shows a sample image of the data.

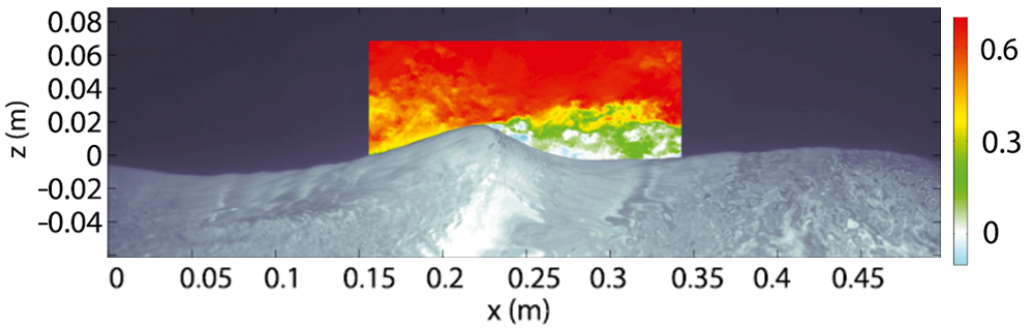

Figure 2: Instantaneous horizontal velocity for the $U_{10} = 9.41$ m s^{-1} wind speed case. Shown is u/U_{10}. Velocity measurments are on a grid with grid spacing of 186 m. Image modified from Buckley and Veron (2016)

The data are categorized by U_{10} equivalent wind speed. For all data sets used in this paper, waves were entirely driven by the overlying wind. U_{10} wind speeds are computed by extrapolating the logarithmic part of the velocity profile. For this analysis, I use data from five different wind speeds: $U_{10} = 0.86$ m s^{-1}, $U_{10} = 2.19$ m s^{-1}, $U_{10} = 5.00$ m s^{-1}, $U_{10} = 9.41$ m s^{-1}. While PIV data were collected for higher wind speed cases, I focus on small wind speeds because (1) they are most interesting for wave growth and (2) they better fit assumptions I make on boundary conditions (see Section 3.4 for details). Table 1 gives a a summary of wave characteristics for each of the four wind speed cases. Values were taken from (Buckley and Veron, 2016).

Table 1: Summary of wave characteristic for each of the wave types studies. U_{10} is the extrapolated U_{10} equivalent wind speed; N is the number of PIV samples; f_p is the peak wave frequency; λ_p is the the wavelength as computed from applying linear wave theory to f_p; and $a = \sqrt{2}\, a_{rms}$, where a_{rms} is the root mean square wave amplitude. Values taken from (Buckley and Veron, 2016)

U_{10} (m s^{-1})	N	a (cm)	λ_p (m)	f_p(Hz)
0.86	1524	–	–	–
2.19	1989	0.15	0.14	3.3
5.00	617	0.50	0.25	2.5
9.41	997	1.20	0.39	2.0

3 Methodology

I use the pressure Poisson equation in order to compute pressure fields from the PIV data. As mentioned above, the data collected by Buckley and Veron (2016) do not have sufficient time resolution to compute the material derivative required for the spatial integration approach. In this subsequent section, I outline the derivation of the pressure Poisson equation and the numerical method I use to solve the Poisson equation. Then, I review the phase-averaging process I use to average the pressure fields. Finally, I describe two different sets of boundary conditions I use to compute the pressure fields.

3.1 Poisson Approach

For incompressible flows ($\nabla \cdot \mathbf{v} = 0$), pressure is related to gradients in velocity according to

$$-\nabla^2 p = f, \tag{1}$$

where

$$f = \rho \nabla \cdot (\mathbf{v} \cdot \nabla \mathbf{v}). \tag{2}$$

Eq. 1 can be derived by taking the divergence of the Navier-Stokes Equations. For a full derivation, see Appendix A. In this paper, I subsequently refer to the function f as the forcing function to the system. This name is suitable since Eq. 1 is analogous to the forced, steady state heat equation. In this context, points with positive f are heat sources whereas points with negative f are heat sinks. In the pressure Poisson problem, this means that regions with $f > 0$ tend to have maxima in pressure whereas regions with $f < 0$ tend to have minima in pressure.

For my analysis, I further simplify the system by assuming that the flow is planar ($v = 0$). This is necessary because the PIV only gives velocity measurements on a plane. The assumption is nontrivial since the flow is turbulent. I show in section 4, however, that on average the deviations from planarity cancel out allowing me to nonetheless obtain realistic average pressure fields. Assuming the flow is planar, the forcing function simplifies to

$$f = -2\rho \left(\frac{\partial u}{\partial x} \frac{\partial w}{\partial z} - \frac{\partial u}{\partial z} \frac{\partial w}{\partial x} \right). \tag{3}$$

Alternate formulations of f are possible due to the planar continuity relationship $\partial u/\partial x = -\partial w/\partial z$. I chose the formulation given by Eq. 3 because it gives an unbiased estimate of f, even when there is noise in the data. For a derivation and explanation of these findings, see Appendix D.

3.2 Numerical Procedure

In order to solve Eq. 1, I use a finite differences scheme on a grid coinciding with the data measurements. Let h_x be the grid spacing in the x-direction and h_z be the grid spacing in the z-direction. Furthermore, let $P_{i,k}$ be the pressure at the i^{th} grid point in the x-direction and the k^{th} grid point in the

z-direction. I then compute the forcing function f at each grid point from the data using Eq. 3. Over the interior of the domain, each grid point is then related to its neighbors by

$$\frac{P_{i+1,\,k} + P_{i-1,\,k} - 2P_{i,\,k}}{h_x^2} + \frac{P_{i,\,k+1} + P_{i,\,k-1} - 2P_{i,\,k}}{h_z^2} = -f_{i,k}. \tag{4}$$

In order to accomodate for the wavy bottom boundary of the computational domain, I discretize the water surface at the bottom of the domain to make it coincide with the grid points. To specify Neumann boundary conditions, I then use appropriate second-order-accurate approximations along the boundary. For Dirichlet boundary conditions, I set the pressure at the nearest boundary point equal to the appropriate value.

3.3 Phase Average

I am are interested determining the pressure that, on average, acts on each part of the wave. This involves, for example, averaging pressure over the wave crest or wave trough at different heights above the water surface. Throughout the rest of the paper, I refer to such an average the *phase average*. In this section, I describe the method I use to phase average data. The water waves in the data are multichromatic and display large variability within wind speeds. First and foremost, phase averaging therefore requires a method of reliably determining wave phase along each part of the water surface.

Figure 3 shows a typical wave profile in a PIV image. I begin the phase averaging process by defining a new coordinate system (ξ, ζ) in the region above the wave. In this coordinate system, the ξ-coordinate is identical to the x-coordinate. The new vertical ordinate ζ, however, measures distance above the water surface (η). Thus

$$\begin{cases} \xi(x,z) &= x \\ \zeta(x,z) &= z - \eta(x). \end{cases} \tag{5}$$

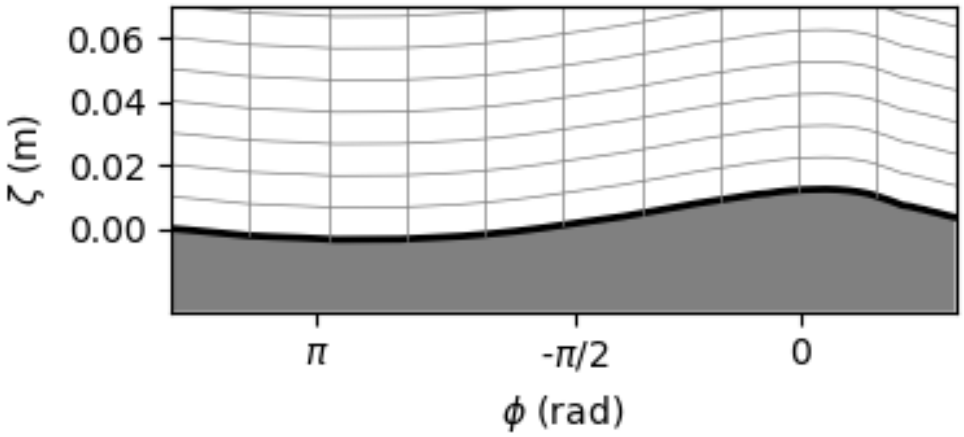

Figure 3: Plot of Coordinate system used during for the analysis. The light gray lines indicate lines of constant ξ and ζ. The thick black line indicates the water surface. Values on the abscissa are wave phases (ϕ), as detected using a Hilbert transform.

I detect wave phases for every ξ-coordinate using a Hilbert transform of the water surface profile. This is identical to the phase detection in Buckley and Veron (2016). A wave phase (ϕ) of 0 denotes the wave crest and a wave phase of $\pm\pi$ denotes the wave trough (see abscissa in Fig. 3). To obtain a phase-average field, I then group the ξ-coordinates into $n = 144$ uniformly sized phase bins covering the interval $-\pi < \phi < \pi$. I average data from all PIV snapshots that are within the same phase bin and at the same height ζ above the water surface. The resultant phase average has the same vertical resolution as the original data but only 144 grid points in the horizontal direction (one per phase bin). The horizontal axis is converted from phase back into distance using the wavelength λ_p given in Table 1.

3.4 Boundary Conditions

As stated by Murai et al. (2007), the Poisson approach is highly sensitive to boundary conditions. The ideal boundary conditions for the flow can be derived by taking the dot product of the Navier-Stokes equations with a normal vector ($\mathbf{n}$) to the boundary. This yields the Neumann-type boundary condition

$$\frac{\mathrm{d}p}{\mathrm{d}\mathbf{n}} = \mathbf{n} \cdot \left(-\rho \frac{\mathrm{D}\mathbf{u}}{\mathrm{D}t} + \mu \nabla^2 \mathbf{v} \right). \tag{6}$$

The problem with this boundary condition is that the data do not have adequate temporal resolution to compute the material derivative $\mathrm{D}\mathbf{u}/\mathrm{D}t$. Furthermore, in order for the Poisson problem to be well posed, I need a Dirichlet boundary condition on at least one point along the boundary. The region of the boundary with a Dirichlet boundary condition must be carefully chosen so as not to skew the final pressure solution.

Given these challenges, I devise two separate methods of computing phase average pressure from the PIV data. In both methods, I make assumptions that make the Poisson problem solvable. While each method has weaknesses, they yield qualitatively similar results suggesting the final solution is valid.

3.4.1 Method 1

In Method 1, I first compute an instantaneous pressure field for each PIV velocity field. I then compute the phase average pressure field by phase averaging all of the instantaneous pressure fields.

Along the top boundary, I use the Dirichlet boundary condition $p = 0$. By using this boundary condition, I assume that wave-induced pressure perturbations have fully decayed by the top boundary. This assumption is a good one for the lower wind speed cases where wave amplitude is much smaller than the height of the computational domain.

On the side boundaries, I use the Neumann condition $\mathrm{d}P/\mathrm{d}\mathbf{n} = 0$. This boundary condition is commonly used in the pressure Poisson problem when exact boundary conditions are not known (Murai et al., 2007). It can be justified by Taylor's frozen turbulence hypothesis and by the fact that pressure fields are known to be smooth.

Finally, along the bottom boundary I use the Neumann condition

$$\frac{\mathrm{d}p}{\mathrm{d}\mathbf{n}} = \mathbf{n} \cdot \left(- \rho_{air} \frac{\mathrm{D}\mathbf{v}}{\mathrm{D}t}\bigg|_{\text{surface}} \right). \tag{7}$$

This equation can be derived from Eq. 6 by neglecting the viscous component. I compute the material derivative $\mathrm{D}\mathbf{v}/\mathrm{D}t$ using a no-slip assumption with the water surface. The acceleration of the water surface is computed using linear wave theory.

Weaknesses of this method are primarily in the top and side boundary conditions. When wave amplitudes are large, the top boundary condition is inaccurate and leads to large errors in the pressure solution. This is the primary reason why I cannot extend my analysis to waves at wind speeds higher than $U_{10} = 9.41$ m s^{-1}. The side boundary condition is problematic when the computational domain has a fin-like region on the sides. In this case, inaccuracies in the side boundary condition strongly skew the pressure solution.

3.4.2 Method 2

In Method 2, I assume that all waves for a given wind speed are identical. Since the Poisson equation is linear, it then follows that I obtain the same phase average pressure field regardless of whether I (1) solve for instantaneous pressure fields first and then phase average or (2) phase average f first and then solve for the pressure field. For a derivation of these results, see Appendix C. While Method 1 takes the former approach, Method 2 takes the latter approach.

In Method 2, I begin by phase-averaging f and then runing the Poissson solver on the result. I now use periodic boundary conditions on the side boundary. This is a natural choice of boundary conditions since phase averages themselves are periodic. For the top boundary, I again use the boundary condition $P = 0$. I observe, however, that phase average f decays rapidly away from the water surface (see section 55.3). This allows me to extend the computational domain upward to a height of 30 cm, setting $f = 0$ in the new regions. By moving the top boundary farther from the water surface, I make the top boundary condition more realistic. Finally, for the bottom boundary (given by the phase-average water surface), I use the same boundary condition as in Method 1 (see Eq. 7).

Method 2 is more robust in terms of the boundary conditions used than Method 1. The computational domain has a larger vertical extent, making the top boundary condition a better approximation. Furthermore the periodic boundary condition on the side is highly appropriate for phase averages and eliminates the problem of fin regions. The primary weakness of this method is that the waves I am dealing with are not identical, as assumed. I nonetheless believe this method yields a close approximation to the phase average.

4 Program Validation: Comparison LES Results

To validate my two methods, I run my Poisson solver on output data from a Large Eddy Simulation (LES) and compare the resulting pressure field with the LES derived pressure field. I assume the LES field is the proper pressure field since it is (1) consistent with the full Navier-Stokes equations and (2) derived at every time step from a 3D consideration of the flow. The latter is important because it allows me to estimate how large of an error results

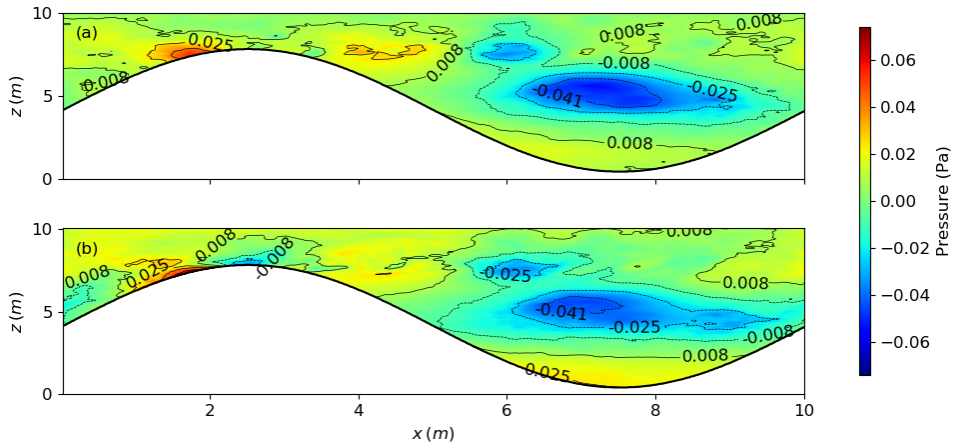

Figure 4: Comparison between (a) the phase averaged pressure field obtained using Method 2 and (b) the average LES pressure field. To ease comparison, both pressure fields are normalized to have mean zero. As can be seen, there is close qualitative agreement between the two pressure fields.

from my assumption that the flow is planar (see Section 3.2).

To reasonably mimic experimental conditions, the LES simulation describes air flowing over a sine-wave mountain. The simulation is run on a square 10 m$\times$5 m$\times$10 m ($x\times y\times z$) grid with grid spacing 0.02 m in all directions. The simulation uses periodic boundary conditions on the side boundaries and Neumann boundary conditions (d/dz = 0) on the top boundary. The mountain is in the shape of a sign wave with amplitude 3.7 m. Unlike a real water wave, the boundary used in the LES simulation does not move with time. To accommodate for this, I replace the bottom boundary condition in my Poisson solver (originally Eq. 7) with the Neumann condition dP/d$\mathbf{n} = 0$. The initial free stream horizontal wind speed used in the model is 2.20 m s^{-1}.

Figure 4(a) shows the resulting phase average pressure field calculated

using Method 2 of the Poisson solver.[1] Figure 4(b) shows the corresponding average pressure field as from the LES simulation. As can be seen in the two panels, there is good agreement between the pressure fields calculated from my Poisson solver and the LES simulation. The average deviation $|P_{LES} - P_{M2}|$ relative to total variation ($\max\{P_{LES}\} - \min\{P_{LES}\}$) is 5%.

The small average deviation between the two pressure fields suggests that my treatment of the flow as planar (see Section 3.2) is unproblematic. Even if the assumption that the flow is planar is not fully satisfied, variations in v cancel out on average allowing me to still get good results for phase average pressure. These findings do not necessarily hold for instantaneous pressure fields. Hence, in this paper, I only present phase-average pressure fields.

5 Results and Discussion

5.1 Phase Average Pressure Fields

Figures 5 and 6 show plots of phase average pressure for each wind speed obtained by methods 1 and 2, respectively. As seen, both methods yield qualitatively similar pressure fields. The pressure fields obtained using Method 1 decay rapidly near the top of the domain. This is due to the effects of the $p = 0$ boundary condition along the top boundary used during this method. For all four wind speeds, the pressure fields are fairly smooth. This is in agreement with my understanding that pressure, even in turbulent flows, is a smooth function (Davidson, 2015). Between each successive wind speed, the pressure perturbations in the airflow increase by a factor of roughly 10.

The $U_{10} = 0.86$ m s^{-1} is the control case since at this wind speed no surface water waves are detectable. Since no waves were detectable, phases

[1]Results shown in Fig. 4 are averages in the y-direction rather than over time. I had trouble downloading enough data (due to the large size of the LES outputs) in order to do time averages. I will repeat the caparison with time average as soon as I find a way to download the data.

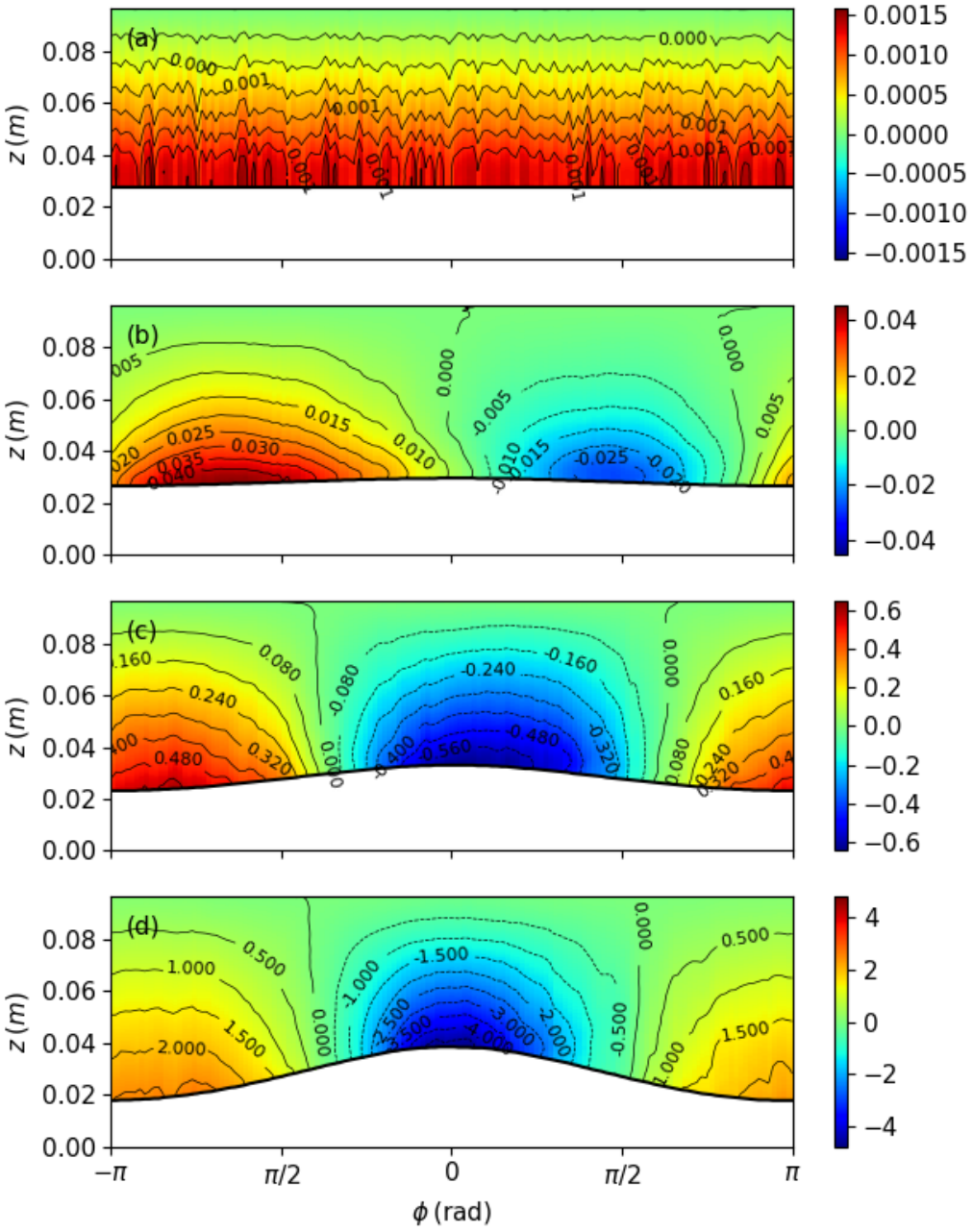

Figure 5: Plot of phase average pressure, as calculated by Method 1, for (a) $U_{10} = 0.86\text{m s}^{-1}$, (b) $U_{10} = 2.19\text{m s}^{-1}$, (c) $U_{10} = 5.00\text{m s}^{-1}$, (d) $U_{10} = 9.41\text{m s}^{-1}$. Shown on the abscissa is wave phase. All pressure fields are in Pascals. Wave as shown are propagating the the right.

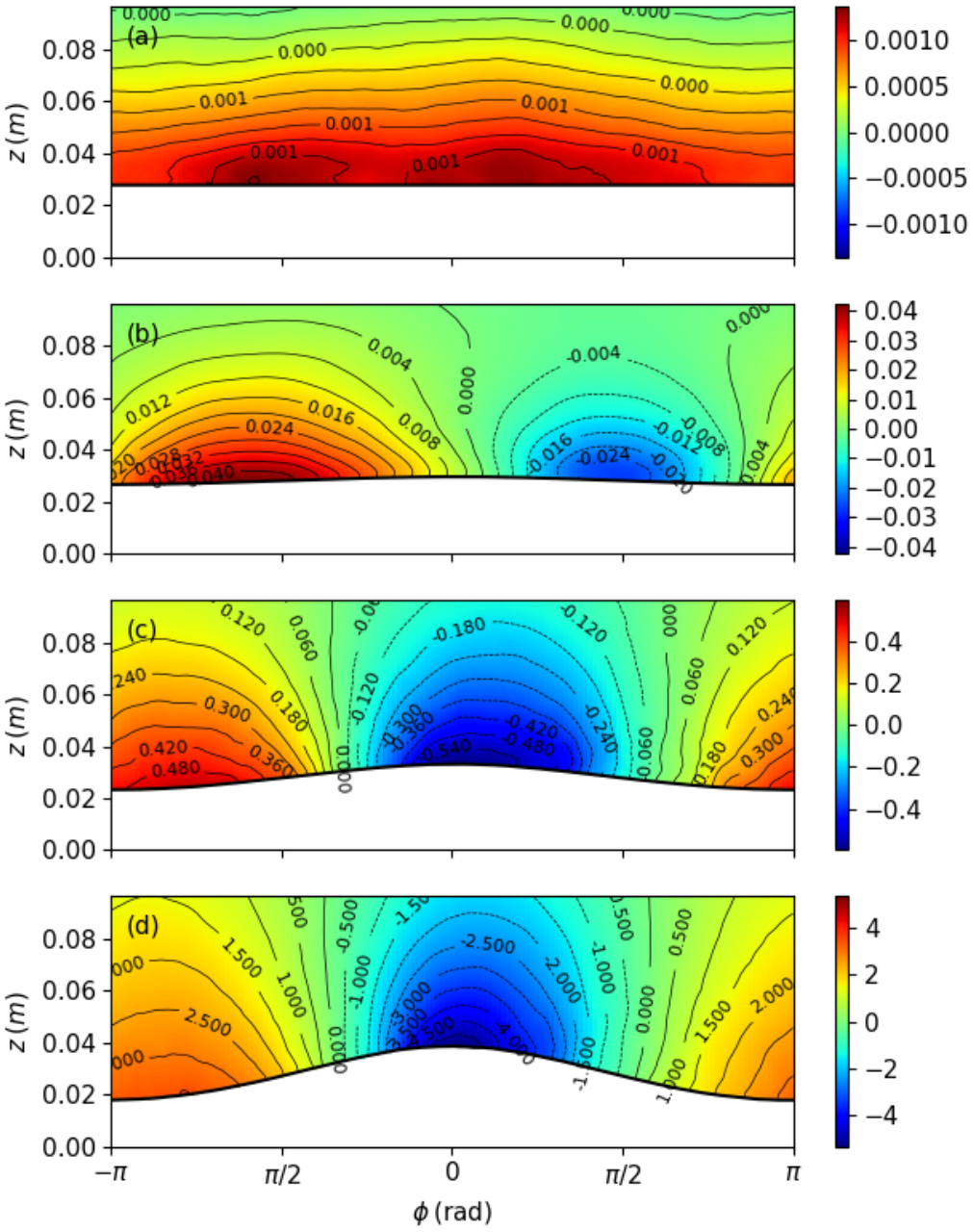

Figure 6: Plot of phase average pressure, as calculated using Method 2 for (a) $U_{10} = 0.86\text{m s}^{-1}$, (b) $U_{10} = 2.19\text{m s}^{-1}$, (c) $U_{10} = 5.00\text{m s}^{-1}$, (d) $U_{10} = 9.41\text{m s}^{-1}$. Shown on the abscissa is wave phase. All pressure fields are in Pascals. Wave as shown are propagating the the right.

were randomly assigned. The pressure field for this case agrees with that of air flowing over a flat horizontal surface. The pressure field is uniform with phase and exists a small negative vertical pressure gradient. The pressure field shown in Fig. 6 is more smooth than the one in 5 since it is the direct output of the Poisson solver rather than an average of instantaneous profiles.

In the $U_{10} = 2.19$ m s^{-1} case, the pressure field is roughly 90° out of phase with the wave. High pressure is found primarily on the windward, upward sloping part of the wave whereas low pressure is found on the leeward, downward sloping part of the wave. Such pressure field is optimal for performing work on water and thus efficient at causing wave growth.

For the two highest wind speed cases the pressure field is out of phase with the water surface. Low pressure regions are located near the wave crests and high pressure regions are located in the wave troughs. I would a similar pressure field over a water-wave oscillating with in an environment no mean mean airflow ($U = 0$). This suggests that part of the pressure field in these larger wave cases is wave-driven rather than wind-driven. Nonetheless, there still seems to be a slight out-of-phase component to these pressure fields. The maximum low pressure is just barely on the leeward of the wave crest while the maximum high pressure is a tiny bit on the windward side of the wave trough. This ensures that the air is still doing work on the water waves.

5.2 Form Drag and Viscous Stress Profiles

Having computed the phase average pressure fields, I verify them by demonstrating that they close the momentum budget for all four wave speeds. According to the law of the wall theory, stress near the water surface is composed entirely of viscous stress and form drag (Kundu and Cohen, 2002). I can thus estimate form drag in two independent ways. First, form drag can be computed by subtracting viscous stress from total stress. Second, form drag can be calculated directly from the phase average pressure fields. In this section, I compute average viscous stress, total stress, and form drag for

each wave and show that they are in agreement with my expectations. In order to do this, I assuming total stress (τ_0) is constant in the entire column.

To calculate total stress, I use

$$\tau_0 = \rho u_*^2. \tag{8}$$

Here u_* is the friction velocity and ρ is air density. According to law of the wall theory, the friction velocity can be estimated from the slope $\mathrm{d}U/\mathrm{d}\log(z)$ in the logarithmic layer of the flow profile. Buckley and Veron (2016) compute friction velocity for each each wind speed by fitting a line of best fit to the logarithmic part of the velocity profile. In this analysis, I use the friction velocities calculated by Buckley and Veron (2016) to calculate total stress. Table 2 shows the friction velocity and total stress for each wind speed.

Table 2: Table of total stress, viscous stress, and form drag for each of the four wind speeds. Form drag was computed using each of the two methods described above.

$U_{10}\,(ms^1)$	u_* (cm s^{-1})	τ_{tot} (Pa m^{-2})	$\frac{\tau_{visc}}{\tau_{tot}}$	$1-\frac{\tau_{visc}}{\tau_{tot}}$	$\frac{\tau_{form}}{\tau_{tot}}$	
					Method 1	Method 2
0.86	2.6	0.0008281	1.33 ± 0.01	-0.33 ± 0.01	-0.0008 ± 0.0007	0.00027
2.19	7.3	0.006528	0.932 ± 0.004	0.068 ± 0.004	0.275 ± 0.008	0.166
5.00	16.7	0.03416	0.590 ± 0.005	0.41 ± 0.005	0.59 ± 0.05	0.367
9.41	31.4	0.1207	0.366 ± 0.003	0.634 ± 0.003	0.77 ± 0.08	0.715

To calculate viscous stress (τ_v), I use the equation for Newtonian fluids that

$$\tau_v = \mu\left(\frac{\partial u}{\partial x} + \frac{\partial w}{\partial z}\right). \tag{9}$$

I compute average values of τ_v within the first 500 μm of the water using PIV data. Figure 7 shows how viscous stress varies along the wave profile for each wind speed. In the control case ($U_{10} = 0.86$ m s^{-1}), there are no detectable

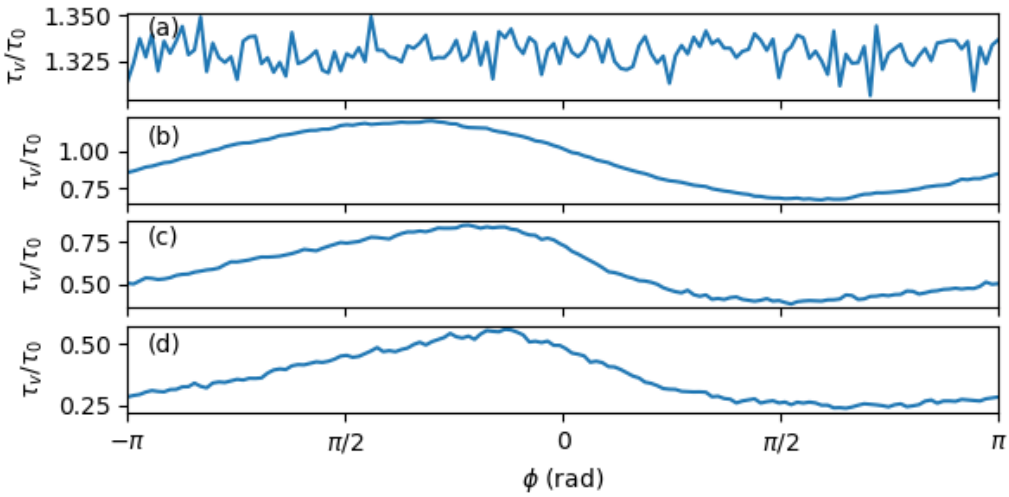

Figure 7: Phase average viscous stress as fraction of total stress versus wave phase for (a) $U_{10} = 0.86$ m s^{-1}, (b) $U_{10} = 2.19$ m s^{-1}, (c) $U_{10} = 5.00$ m s^{-1}, and (d) $U_{10} = 9.41$ m s^{-1}.

waves and hence viscous stress is nearly constant with phase. In the other wind speeds, viscous stress peaks slightly windward of the wave crest. This is consistent with the finding of (Buckley, 2015) that the boundary layer is thinnest near the wave crest. A thin boundary layer means that velocity shear is large since u approaches its free stream veloicty rapidly with altitude. The point of maximum viscous stress moves closer to the wave crest as wind speed increases. The minimum viscous stress, on the other hand, occurs on the leeward side of the wave near wave phase $\pi/2$. Minimum viscous stress likely occurs in this region since it is the region that is most sheltered by the wave. Table 2 shows the overall average viscous stress for each wave type. Uncertainties in average viscous stresses are calculated using a bootstrap algorithm.

Finally, I calculate form drag (τ_f) directly from the pressure field using

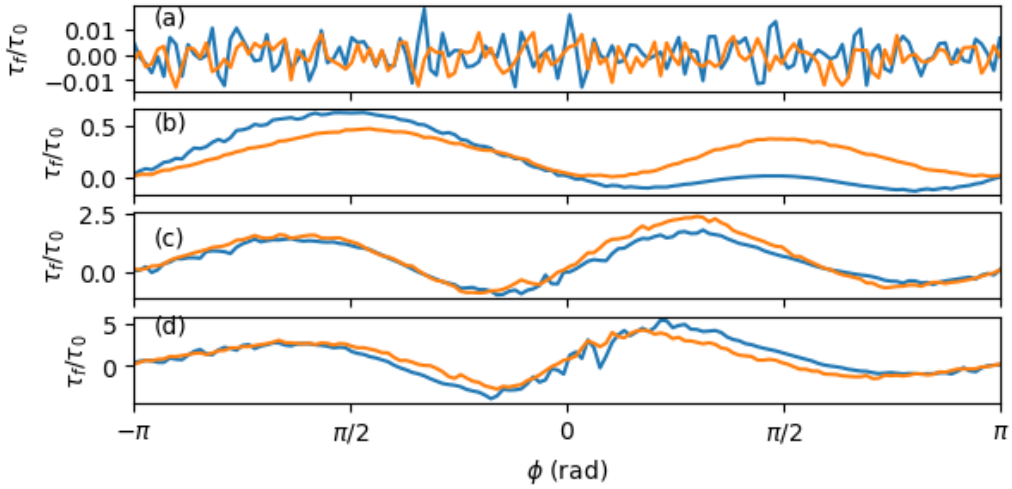

Figure 8: Phase average form drag as fraction of total stress versus wave phase for (a) $U_{10} = 0.86$ m s^{-1}, (b) $U_{10} = 2.19$ m s^{-1}, (c) $U_{10} = 5.00$ m s^{-1}, and (d) $U_{10} = 9.41$ m s^{-1}. Orange lines show the form drag computed by Method 1 (running the solver on instantenous PIV fields) and blue lines show the form drag computed for Method 2 (running the solver on phase average f).

the pressure slope correlation (Grare et al., 2013):

$$\tau_f = \left\langle p_s \frac{\mathrm{d}\eta}{\mathrm{d}x} \right\rangle. \tag{10}$$

Here, η is the height of the water surface, p_s is surface pressure, and $< \cdot >$ denotes an average over all phases. Figure 8 shows how pressure slope correlation varies with phase for each wave type. As can be seen, pressure slope correlation increases relative to total stress with increasing wind speed. For the control case with no detectable wave ($U_{10} = 0.86$ m s^{-1}), the pressure-slope correlation fluctuates around zero with no consistent structure. This agrees with my understanding that turbulent surface pressure variations are random for flow over a flat surface. For the $U_{10} = 2.19$ m s^{-1} wind speed case, the pressure slope correlation has a global maximum on the windward side of

the wave. This suggests wave growth is driven primarily by the high pressure region on the windward, upward sloping part of the wave. Finally, for the two highest wind speed cases ($U_{10} = 5.00$ m s^{-1} and $U_{10} = 9.41$m s^{-1}), the pressure slope correlation has a global maximum on the leeward side of the wave. Wave growth for these waves is thus primarily driven by the low pressure region in the wake of the wave crest. This is consistent with the existence of airflow separation for flow over large waves (Buckley, 2015). Nonetheless, pressure slope correlation still has a local maximum on the windward side of the wave, suggesting that this region still contributes to wave growth.

As shown in Table 2, the form drag (τ_f/τ_0) calculated using Method 2 agrees to within about 10% of that expected from $(\tau_0 - \tau_v)/\tau_0$ for the three larger wind speeds. This further validates that the pressure fields I computed are reasonable. For the smallest wind speed ($U_{10} = 0.86$ m s^{-1}), the disagreement is 33%. This, however, is because $\tau_v > \tau_0$. My computed form drag is nearly zero, which makes sense for a flat water surface.

Method 1 consistently overestimates form drag, suggesting that Method 2 is the better approach. This may be explained by the fact that Method 1 is more is heavily affected by fin-like regions on the side the computational domain. By fin-like regions, I mean regions where the boundary forms an acute angle. In such regions, errors in boundary conditions often cause extreme values in pressure, which may explain why form drag estimates are too high. Further experimentation is necessary, however, to confirm these findings.

5.3 Analysis of Phase Average f

In this section, I proceed to investigate which features of the airflow lead to the described high and low pressure regions. In order to do this, I investigate phase average f for each wave profile. As mentioned in section 33.1, the forcing function in the pressure Poisson problem is analogous to the distribution of heat sources and sinks in the steady-state heat equation. Regions where f is positive produce pressure maxima whereas regions where f is negative

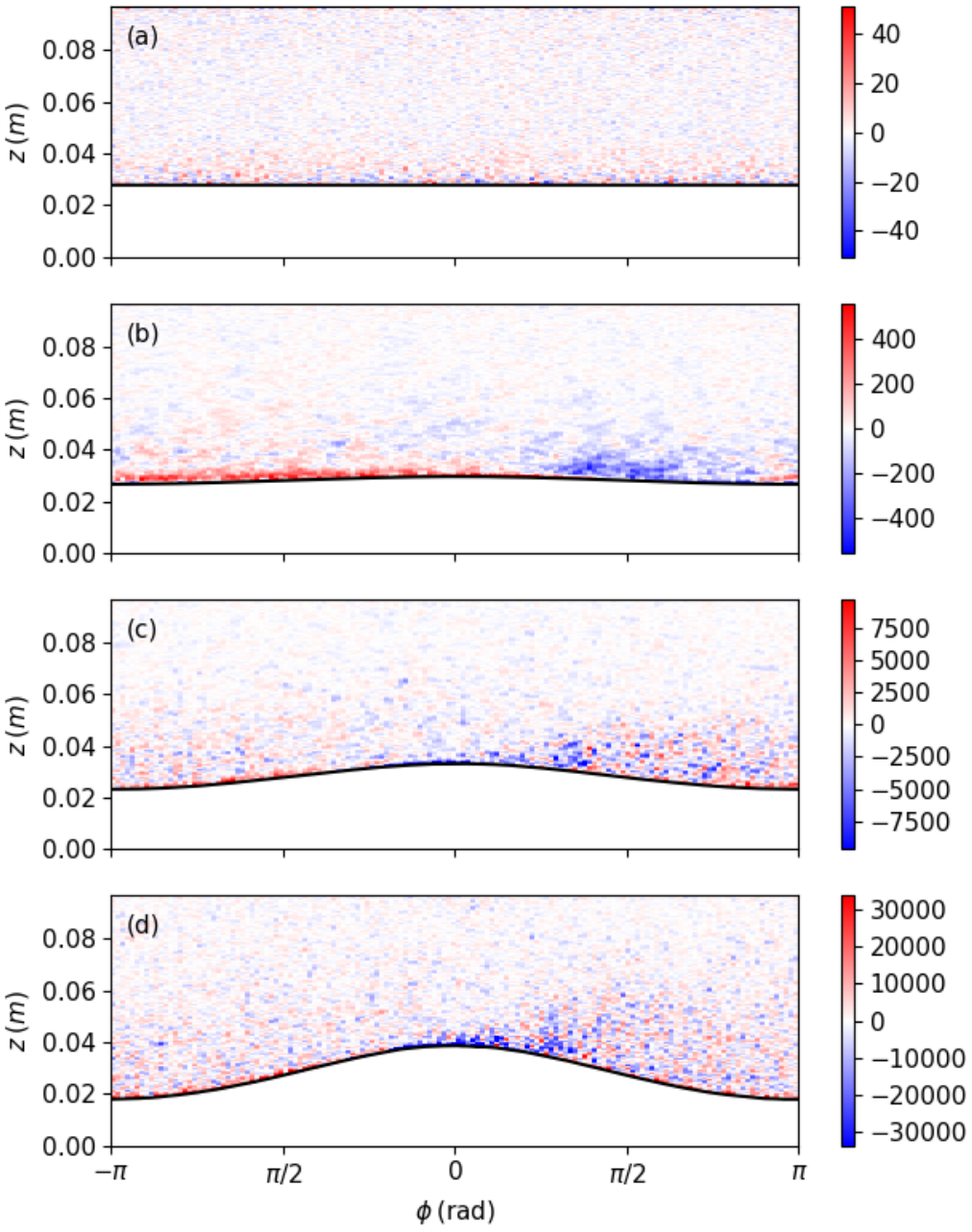

Figure 9: Plot of phase average f for (a) $U_{10} = 0.86$ m s^{-1}, (b) $U_{10} = 2.19$ m s^{-1}, (c) $U_{10} = 5.00$ m s^{-1}, (d) $U_{10} = 9.41$ m s^{-1}. Shown on the abscissa is wave phase. Units of f are Pa m^{-2} in all plots.

produce pressure minima.

Figure 9 shows a plot of phase average f for each wind speed. For the control wind speed case ($U_{10} = 0.86$ m s^{-1}), the plot of phase average f looks random. This agrees with my expectation that for this wind speed variations in pressure are entirely due to turbulence. Next, for the $U_{10} = 2.19$ m s^{-1} case, $f > 0$ on the windward side of the wave and $f < 0$ on the leeward side. Interestingly, the regions with largest f are a tiny bit above the water surface rather than directly at the water surface. This agrees with the wave growth theory by Miles (1957), which states that momentum transfer into the water is controlled by the velocity profile at the height where u equals the wave speed c. Finally, for the two largest wind speeds, phase average f has no consistent structure except (1) small patches of $f > 0$ directly on the water surface of the windward side of the wave and (2) a region where $f < 0$ directly leeward of the wave crest. The similarity in phase average f between the two largest wind speeds suggests that similar mechanisms are driving wave growth in each case.

To further investigate the origin of the observed pressure fields, I break down f into various distinct, identifiable components. The forcing function can rewritten as (Davidson, 2015):

$$\begin{aligned} f &= -2\rho\left(\frac{\partial u}{\partial x}\frac{\partial w}{\partial z} - \frac{\partial u}{\partial z}\frac{\partial w}{\partial x}\right) \\ &= 2\rho\left[\left(\underbrace{\frac{\partial u}{\partial x}}_{\substack{\text{linear}\\ \text{strain}}}\right)^2 + \left(\underbrace{\frac{1}{2}\left[\frac{\partial u}{\partial z} + \frac{\partial w}{\partial x}\right]}_{\substack{\text{shear}\\ \text{strain}}}\right)^2 - \left(\underbrace{\frac{\omega}{2}}_{\text{vorticity}}\right)^2\right]. \end{aligned} \tag{11}$$

In the above formulation, the first term depends only on the linear strain rate. This term thus relates to stretching of fluid elements along their direction of motion. It is always positive, suggesting that such stretching induces pressure maxima. The second term in Eq. 11 depends only on the shear strain rate. Shear strain describes the rate at which two initially perpen-

dicular line segments are rotated toward each other in the flow (Kundu and Cohen, 2002). Again, the second term is always positive indicating that shear strain leads to maxima in pressure. Finally, the third term depends only on vorticity, $\omega = \partial w/\partial x - \partial u/\partial z$. Vorticity is related to circulation in the flow via Stokes theorem (see Kundu and Cohen (2002)) and is thus related to rotational motion in the fluid. The third term is always negative and is the only negative component in f. Hence, all minima in pressure are caused by vorticity within the fluid. Eq. 11 can thus be interpreted as a trade off between strain (high pressure inducing) and vorticity (low pressure inducing).

In the airflows above water waves, shear strain and vorticity are highly correlated. This is because $\partial u/\partial z >> \partial w/\partial z$. I thus consider terms two and three in Eq. 11 together rather than separately. In the subsequent analysis, I therefore decompose f into two terms:

$$\chi_1 = 2\rho\left(\frac{\partial u}{\partial x}\right)^2 \tag{12}$$

$$\chi_2 = 2\rho\left[\left(\frac{1}{2}\left[\frac{\partial u}{\partial z} + \frac{\partial w}{\partial x}\right]\right)^2 - \left(\frac{\omega}{2}\right)^2\right] \tag{13}$$

Term 1 (χ_1) describes the effect of linear strain on pressure. Term 2 (χ_2) represents the trade-off between shear strain and vorticity on pressure. When $\chi_2 > 0$, shear strain dominates over vorticity, wheras if $\chi_2 < 0$ then vorticity dominates over shear strain.

Figure 10 shows how χ_1 and χ_2 vary along the wave profile. Values shown are averages over the first 2 mm of the surface. For the $U_{10} = 0.86$ m s^{-1} wind speed case f fluctuates around zero near the water surface with no consistent structure. Fluctuations in f are dominated by the χ_2 term. This suggests that fluctuations in pressure are controlled by shear strain and vorticity within the fluid. Linear strain plays a negligable in determining pressure. This agrees with my expectation since flow over the flat water surface is unobstructed and only contains small turbulent eddies.

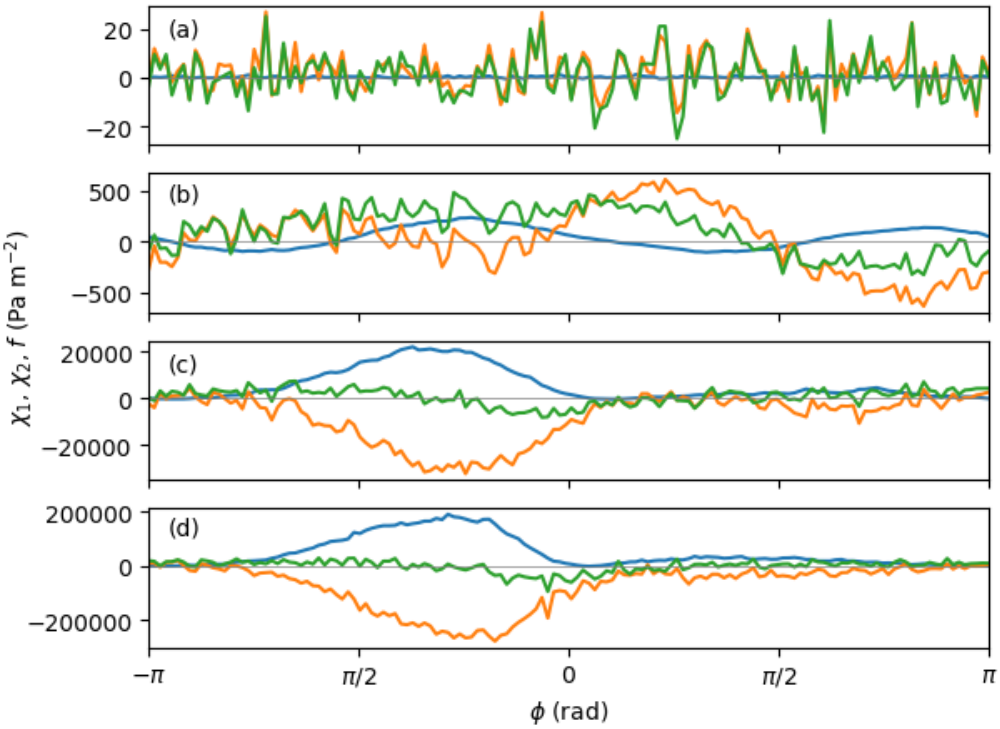

Figure 10: Plot of χ_1 (blue), χ_2 (orange), and f (green) versus wave phase for each of the wave cases. Panel (a) $U_{10} = 0.86$ m s^{-1}, (b) $U_{10} = 2.19$ m s^{-1}, (c) $U_{10} = 5.00$ m s^{-1}, (d) $U_{10} = 9.41$ m s^{-1}. Units of χ_1, χ_2, and f are Pa m^{-2} in all plots. Values shown are averages within the first 2 mm of the water surface.

For the $U_{10} = 2.19$ m s^{-1} wind speed case, the high pressure region on the windward side of the wave is caused by (i) strong shear strain in the wave trough (positive χ_2) and (ii) positive linear strain near the wave crest (positive χ_1). The only region along the water surface where $f < 0$ is on the leeward side of the wave, near the wave trough. Negative pressure in this region is caused by high vorticity relative to shear strain (negative χ_2).

For the two larger wind speeds cases ($U_{10} = 5.00$ m s^{-1} and $U_{10} = 9.41$ m s^{-1}), I see very different dynamics. In the wave trough, high pres-

sure is caused by strong shear strain. Moving up the wave on the windward side, pressure continues to remain high due to increasing linear strain in the airflow. Linear strain is maximum on the windward side of the wave near the wave crest. This is compensated, however, by high vorticity near the wave crest. The net effect is a low pressure region near the wave crest due to vorticity dominating over linear strain. This extends down the leeward side of the wave.

6 Conclusion

In this paper, I develop a methodology to compute phase-average pressure fields over water waves from PIV data. I verify my methodology using LES simulation data and a bulk analysis of stresses. I find that at $U_{10} = 2.19$ m s^{-1}, the pressure field is roughly 90° out of phase with the water surface. This is optimal for doing work on the water. At higher wind speeds, the pressure field is out of phase with the water surface, with low pressure regions on the wave crest and high pressure in the wave trough. Nonetheless, there is a slight phase shift in the pressure field still allows work to be done on the water.

Empirically derived pressure fields can help verify or reject existing wave growth theories. With further analysis, I can use them to trace exactly which turbulent structures within the airflow above waves lead to wave growth. This will help increase not only understanding of wave growth, but also understanding of atmosphere ocean interactions.

Further work needs to be done to extend this analysis to a larger array of wave types. At present, I was only able to compute pressure fields for waves with small amplitudes due to limitations in boundary conditions. Carefully engineered PIV setups with better temporal resolution and covering a larger domain will allow this analysis to be extended to a larger variety of wave types. Similarly, PIV setups in the field may allow determination of pressure

fields over real ocean waves rather than laboratory ones.

7 Acknowledgments

Special thank you to Jeff Carpenter and Mary-Louise Timmermans for supervising my project. The amount of time you have dedicated to me has truly means a lot. You both make me feel very at home in the scientific community. Thank you also to Marc Buckley for providing me with the PIV data introducing me to to the bulk stress analysis. Finally, thank you to Larissa Schultze her time spent running the LES simulations.

Appendices

A Derivation of the Pressure Poisson Equation

Here, I will show the derivation of the pressure Poisson equation. I begin with the Navier-Stokes equations:

$$\nabla p = \rho\Big(- \frac{\mathrm{D}\mathbf{v}}{\mathrm{D}t} + \nu\nabla^2\mathbf{v}\Big) \tag{A1}$$

Taking the divergence of both sides, I get

$$\begin{aligned}
\nabla^2 p &= \nabla\cdot\Big[\rho\Big(- \frac{\mathrm{D}\mathbf{v}}{\mathrm{D}t} + \nu\nabla^2\mathbf{v}\Big)\Big] \\
&= \rho\nabla\cdot\Big(- \frac{\mathrm{D}\mathbf{v}}{\mathrm{D}t} + \nu\nabla^2\mathbf{v}\Big) + \nabla\rho\cdot\Big(- \frac{\mathrm{D}\mathbf{v}}{\mathrm{D}t} + \nu\nabla^2\mathbf{v}\Big) \\
&= \rho\Big[- \frac{\partial(\nabla\cdot\mathbf{v})}{\partial t} - \nabla\cdot(\mathbf{v}\cdot\nabla\mathbf{v}) + \nu\nabla^2(\nabla\cdot\mathbf{v})\Big] + \frac{\nabla\rho\cdot\nabla p}{\rho} \\
&= -\rho\nabla\cdot(\mathbf{v}\cdot\nabla\mathbf{v}) + \frac{\nabla\rho\cdot\nabla p}{\rho}
\end{aligned} \tag{A2}$$

The last step follows by assuming that the flow is incompressible ($\nabla\cdot\mathbf{v} = 0$). I now further assume that

$$\left|\frac{\nabla\rho\cdot\nabla p}{\rho}\right| << \left|\rho\nabla\cdot(\mathbf{v}\cdot\nabla\mathbf{v})\right| \tag{A3}$$

which follows from the fact that $\nabla\rho/\rho$ is small for incompressible flows. Under this additional assumption, Eq. A2 becomes:

$$-\nabla^2 p = \rho\nabla\cdot(\mathbf{v}\cdot\nabla\mathbf{v}) \tag{A4}$$

Eq. A4 is the Poisson Equation used in this paper to solve for pressure. Assuming the flow is planar ($v = 0$), Eq. A4 further simplifies to simplifies to

$$-\nabla^2 p = -2\rho\left(\frac{\partial u}{\partial x}\frac{\partial w}{\partial z} - \frac{\partial u}{\partial z}\frac{\partial w}{\partial x}\right) \tag{A5}$$

B Proof That f is Unbiased

For computing pressure fields, it is important that the data give an accurate estimate of the forcing function f. If the computed value of f is consistently higher or lower than the true value, then the resultant pressure field will be heavily skewed.

I show here that Eq. 3 is unbaised. Unbiased means that, given random noise in the data, the expected value of the forcing function ($\mathbb{E}f$) equals the true value of the forcing function ($\tilde{f}$). Assume that at each grid point, any measured velocity gradient (M) equals the true gradient ($\tilde{M}$) plus some random noise (δ_M) i.e.

$$M = \tilde{M} + \delta_M. \tag{B1}$$

Furthermore, that assume that noise has mean zero ($\mathbb{E}\delta_M = 0$) and that noise in all gradients are independent of one another. Then

$$\begin{aligned}
\mathbb{E}f &= -2\rho\mathbb{E}\left[\frac{\partial u}{\partial x}\frac{\partial w}{\partial z} - \frac{\partial u}{\partial z}\frac{\partial w}{\partial x}\right] \\
&= -2\rho\mathbb{E}\left[\left(\widetilde{\frac{\partial u}{\partial x}} + \delta_{\frac{\partial u}{\partial x}}\right)\left(\widetilde{\frac{\partial w}{\partial z}} + \delta_{\frac{\partial w}{\partial z}}\right) - \left(\widetilde{\frac{\partial u}{\partial z}} + \delta_{\frac{\partial u}{\partial z}}\right)\left(\widetilde{\frac{\partial w}{\partial x}} + \delta_{\frac{\partial w}{\partial x}}\right)\right] \\
&\overset{(a)}{=} -2\rho\left(\widetilde{\frac{\partial u}{\partial x}}\widetilde{\frac{\partial w}{\partial z}} + \widetilde{\frac{\partial u}{\partial z}}\widetilde{\frac{\partial w}{\partial x}}\right) + \mathbb{E}\left(\delta_{\frac{\partial u}{\partial x}}\delta_{\frac{\partial w}{\partial z}} + \delta_{\frac{\partial w}{\partial z}}\delta_{\frac{\partial u}{\partial z}}\right) \\
&\overset{(b)}{=} \tilde{f} + \left(\mathbb{E}\delta_{\frac{\partial u}{\partial x}}\,\mathbb{E}\delta_{\frac{\partial w}{\partial z}} + \mathbb{E}\delta_{\frac{\partial w}{\partial z}}\,\mathbb{E}\delta_{\frac{\partial u}{\partial z}}\right) \\
&= \tilde{f}.
\end{aligned} \tag{B2}$$

Here, step (a) follows by expanding all terms and using linearity of expection. Step (b) follows using the fact that for independent random variables X and

Y, $\mathbb{E}(XY) = \mathbb{E}X\mathbb{E}Y$. Equation B2 implies that my estimate of f is unbiased.

For other expression of f are not unbiased. For example, Van Oudheusden (2013) gives the equation of f as

$$f = \rho\left[\left(\frac{\partial u}{\partial x}\right)^2 - 2\frac{\partial u}{\partial z}\frac{\partial w}{\partial x} + \left(\frac{\partial w}{\partial z}\right)^2\right]. \tag{B3}$$

According to the planar continuity relationship ($\partial u/\partial x = -\partial w/\partial z$), Equation B3 is equivalent to Eq. 3. Using an analysis similar to the one presented above, however, I can show that Eq. B3 gives a positively biased estimate of f. The magnitude of the positive bias depends on the variance of the noise $\delta_{\frac{\partial u}{\partial x}}$ and $\delta_{\frac{\partial w}{\partial z}}$. Figure B1 shows a histogram of f at all grid points for a single PIV snapshot, as estimated using both methods. The positive skew in f when estimated by Eq. B3 is clearly visible.

C Phase Average Pressure from Poisson Equation

Assume that all waves for a given wind speed are identical in shape. Under this assumption, I show that phase average pressure can be computed by running the Poisson Solver on phase average f.

Let Ω denote the region measured region in the flow. If all water waves for a given wind speed have the same shape, then Ω is identical in shape for all PIV velocity fields. Consider now solving a series of pressure Poisson problems given by

$$\begin{cases} -\nabla^2 p_i = f_i, & \text{for } \mathbf{x} \in \Omega \\ \frac{\partial p_i}{\partial \mathbf{n}} = g(\mathbf{x}) & \text{for } \mathbf{x} \in \Gamma_1 \subseteq \partial\Omega \\ p_i = d(\mathbf{x}) & \text{for } \mathbf{x} \in \Gamma_2 \subseteq \partial\Omega. \end{cases} \tag{C1}$$

Here , p_i and f_i are the pressure and forcing function corresponding to the i^{th} PIV velocity field; $\partial\Omega$ is the boundary of the domain Ω; $\Gamma_1 \subseteq \partial\Omega$ is the set

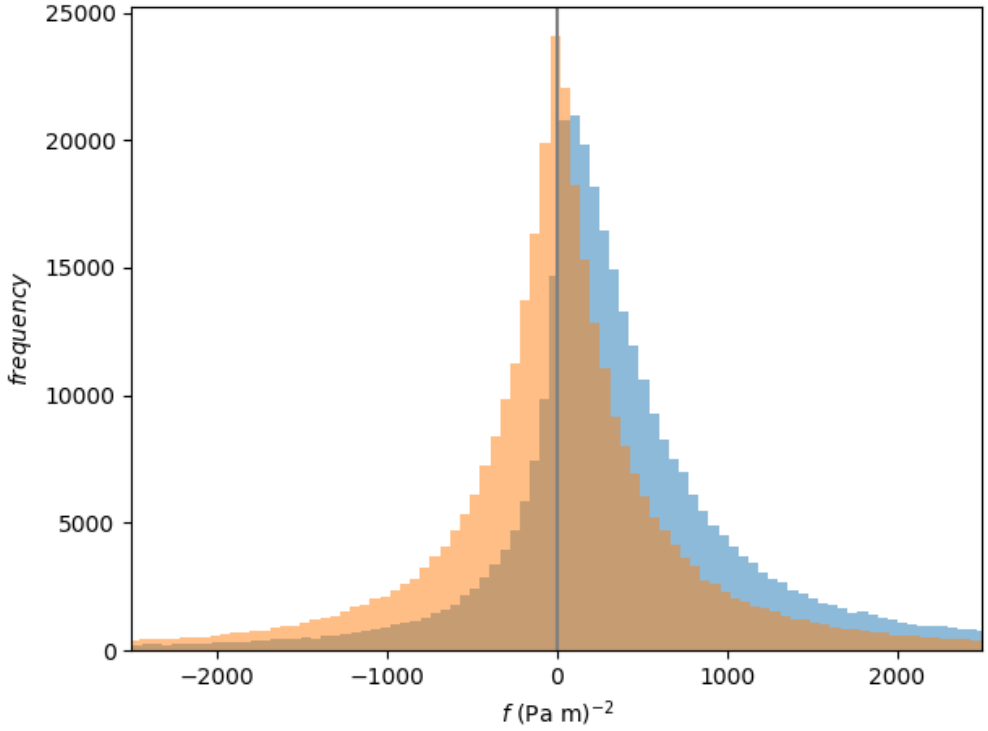

Figure B1: Histograms of f at every gridpoint for one PIV snapshot of the $U_{10} = 2.19$ m s^{-1} wind speed. Shown in orange is f and calculated using Eq. 3. Shown in blue is f as calculated using B3.

of boundary points with Neumann boundary conditions and $\Gamma_2 \subseteq \partial\Omega$ is the set of boundary points with Dirichlet boundary conditions ($\Gamma_1 \cup \Gamma_2 = \partial\Omega$).

Consider now computing the average pressure $\overline{p}$ over all flow fields. I can then show the phase average pressure satisfies all of the properties given in Eq. C1 for instantaneous pressure fields. For $\mathbf{x} \in \Omega$

$$-\nabla^2\overline{p} = -\nabla^2\left(\frac{1}{N}\sum_i p_i\right) = \frac{1}{N}\sum_i(-\nabla^2 p_i) = \frac{1}{N}\sum_i f_i = \overline{f}. \qquad \text{(C2)}$$

Furthermore, for $\mathbf{x} \in \Gamma_1$

$$\frac{\partial \overline{p}}{\partial \mathbf{n}} = \frac{\partial}{\partial \mathbf{n}}\left(\frac{1}{N}\sum_i p_i\right) = \frac{1}{N}\sum_i \left(\frac{\partial p_i}{\partial \mathbf{n}}\right) = \frac{1}{N}\sum_i g(\mathbf{x}) = g(\mathbf{x}). \tag{C3}$$

Finally, for $\mathbf{x} \in \Gamma_2$

$$\overline{p} = \frac{1}{N}\sum_i p_i = \frac{1}{N}\sum_i d(\mathbf{x}) = d(\mathbf{x}). \tag{C4}$$

Combining Eq. C2, C3 and C4, I have that $\overline{p}$ is the solution to the problem

$$\begin{cases} -\nabla^2 \overline{p} = \overline{f}, & \text{for } \mathbf{x} \in \Omega \\ \frac{\partial \overline{p}}{\partial \mathbf{n}} = g(\mathbf{x}) & \text{for } \mathbf{x} \in \Gamma_1 \subseteq \partial\Omega \\ \overline{p} = d(\mathbf{x}) & \text{for } \mathbf{x} \in \Gamma_2 \subseteq \partial\Omega. \end{cases} \tag{C5}$$

This problem is identical to the one used to compute instantaneous pressure fields (Eq. C1), except that the instantaneous forcing function is now replaced by the phase average forcing function f. It follows that I can obtain the phase average pressure by running the Poisson solver on phase average f. This forms the basis of my second method of computing the phase average pressure.

D Instantaneous Pressure Fields

In the main thesis, I only present the phase average pressure fields for each wind speed. In this section, I give an example instantaneous pressure fields. The instantaneous pressure fields were computed using the boundary conditions of Method 1 (see Section 3.4). They show a tremendous amount of variation and do no necessarily correspond well with the phase average pressure fields. Figures D1-D4 show example instantaneous pressure fields. All pressure fields are normalized to have mean zero.

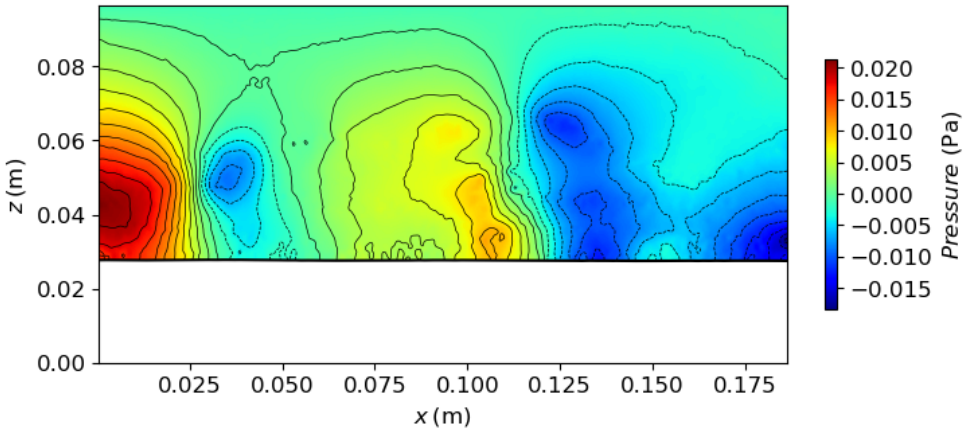

Figure D1: Example instantaneous pressure field over a water wave for the $U_{10} = 0.86$ m s^{-1} wind speed case. Air is flowing to the right. The wave is also propagating to the right.

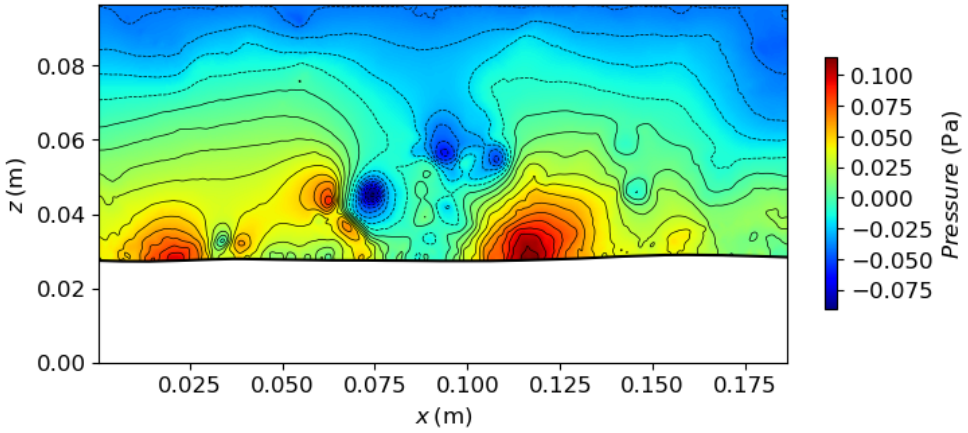

Figure D2: Example instantaneous pressure field over a water wave for the $U_{10} = 2.19$ m s^{-1} wind speed case. Air is flowing to the right. The wave is also propagating to the right.

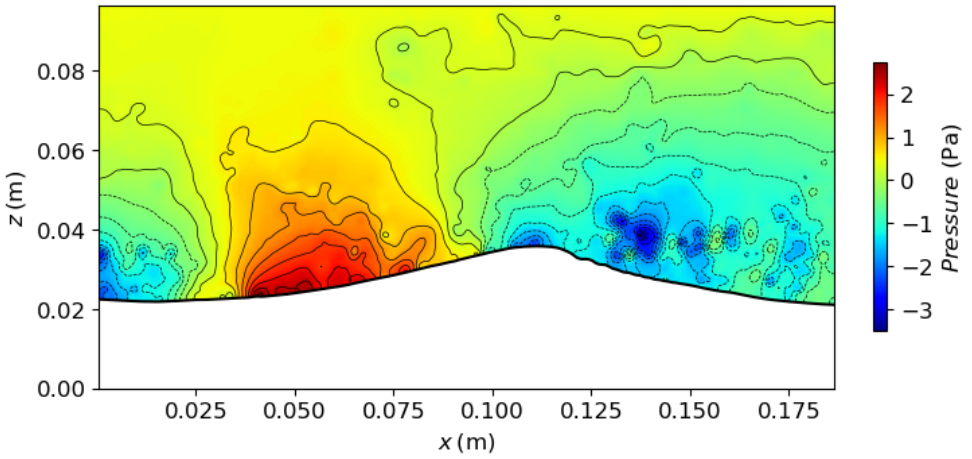

Figure D3: Example instantaneous pressure field over a water wave for the $U_{10} = 5.00$ m s^{-1} wind speed case. Air is flowing to the right. The wave is also propagating to the right.

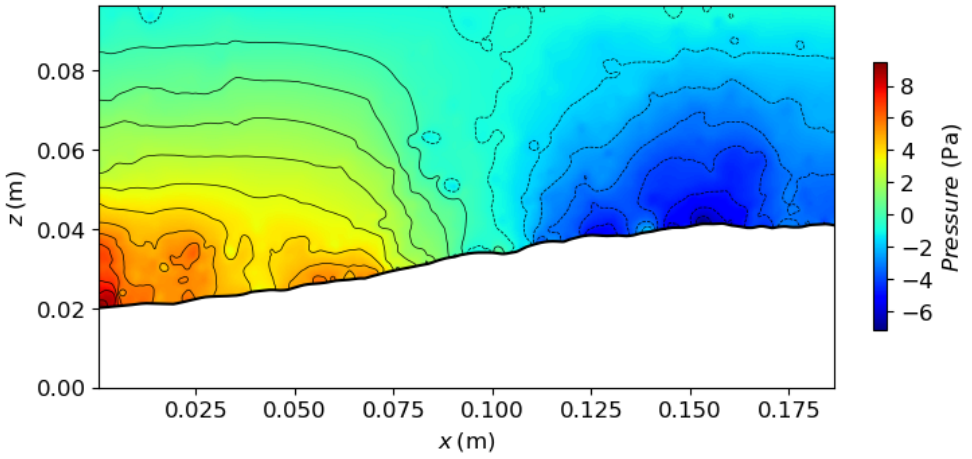

Figure D4: Example instantaneous pressure field over a water wave for the $U_{10} = 9.41$ m s^{-1} wind speed case. For this wind speed, the PIV imaging area is not large enough to cover an entire wavelength of the wave. Air is flowing to the right. The wave is also propagating to the right.

References

Baur, T. Piv with high temporal resolution for the determination of local pressure reductions from coherent turbulence phenomena. In *Proc. 3rd Int. Workshop on PIV-Santa Barbara*, pages 101–106, 1999.

Buckley, M. *Structure of the Airflow Above Surface Water Waves*. PhD thesis, University of Delaware, 2015.

Buckley, M. P. and Veron, F. Structure of the airflow above surface waves. *Journal of Physical Oceanography*, 46(5):1377–1397, 2016.

Davidson, P. *Turbulence: an introduction for scientists and engineers*. Oxford University Press, 2015.

Eckart, C. The generation of wind waves on a water surface. *Journal of Applied Physics*, 24(12):1485–1494, 1953.

Fujisawa, N., Tanahashi, S., and Srinivas, K. Evaluation of pressure field and fluid forces on a circular cylinder with and without rotational oscillation using velocity data from piv measurement. *Measurement Science and Technology*, 16(4):989, 2005.

Grare, L., Peirson, W. L., Branger, H., Walker, J. W., Giovanangeli, J.-P., and Makin, V. Growth and dissipation of wind-forced, deep-water waves. *Journal of Fluid Mechanics*, 722:5–50, 2013.

Helmholtz, P. Xliii. on discontinuous movements of fluids. *The London, Edinburgh, and Dublin Philosophical Magazine and Journal of Science*, 36 (244):337–346, 1868.

Jakobsen, M., Dewhirst, T., and Greated, C. Particle image velocimetry for predictions of acceleration fields and force within fluid flows. *Measurement Science and Technology*, 8(12):1502, 1997.

Jeffreys, H. On the formation of water waves by wind. *Proceedings of the Royal Society of London. Series A, Containing Papers of a Mathematical and Physical Character*, 107(742):189–206, 1925.

Klein, C., Engler, R. H., Henne, U., and Sachs, W. E. Application of pressure-sensitive paint for determination of the pressure field and calculation of the forces and moments of models in a wind tunnel. *Experiments in Fluids*, 39 (2):475–483, 2005.

Kundu, P. K. and Cohen, I. M. *Fluid mechanics*. Academic Press, 2002.

Liu, X. and Katz, J. Instantaneous pressure and material acceleration measurements using a four-exposure piv system. *Experiments in Fluids*, 41(2): 227, 2006.

Miles, J. W. On the generation of surface waves by shear flows. *Journal of Fluid Mechanics*, 3(2):185–204, 1957.

Murai, Y., Nakada, T., Suzuki, T., and Yamamoto, F. Particle tracking velocimetry applied to estimate the pressure field around a savonius turbine. *Measurement Science and Technology*, 18(8):2491, 2007.

Phillips, O. M. On the generation of waves by turbulent wind. *Journal of fluid mechanics*, 2(5):417–445, 1957.

Schwabe, M. Über druckermittlung in der nichtstationären ebenen strömung. *Ingenieur-Archiv*, 6(1):34–50, 1935.

Sullivan, P. P., McWilliams, J. C., and Moeng, C.-H. Simulation of turbulent flow over idealized water waves. *Journal of Fluid Mechanics*, 404:47–85, 2000.

Sullivan, P. P., Banner, M. L., Morison, R. P., and Peirson, W. L. Turbulent flow over steep steady and unsteady waves under strong wind forcing. *Journal of Physical Oceanography*, 48(1):3–27, 2018.

Thompson, W. S. Hydrokinetic solutions and observations. *Phil. Mag.*, (4): 374, 1871.

Van Oudheusden, B. Piv-based pressure measurement. *Measurement Science and Technology*, 24(3):032001, 2013.

Willert, C. E. and Gharib, M. Digital particle image velocimetry. *Experiments in fluids*, 10(4):181–193, 1991.

Yang, D. and Shen, L. Direct-simulation-based study of turbulent flow over various waving boundaries. *Journal of Fluid Mechanics*, 650:131–180, 2010.

Yang, Z., Deng, B.-Q., and Shen, L. Direct numerical simulation of wind turbulence over breaking waves. *Journal of Fluid Mechanics*, 850:120–155, 2018.